

A surgical robot with augmented reality visualization for stereoelectroencephalography electrode implantation

Bowei Zeng¹ · Fanle Meng¹ · Hui Ding¹ · Guangzhi Wang¹

Received: 11 January 2017 / Accepted: 17 June 2017 / Published online: 29 June 2017
© CARS 2017

Abstract

Purpose Using existing stereoelectroencephalography (SEEG) electrode implantation surgical robot systems, it is difficult to intuitively validate registration accuracy and display the electrode entry points (EPs) and the anatomical structure around the electrode trajectories in the patient space to the surgeon. This paper proposes a prototype system that can realize video see-through augmented reality (VAR) and spatial augmented reality (SAR) for SEEG implantation. The system helps the surgeon quickly and intuitively confirm the registration accuracy, locate EPs and visualize the internal anatomical structure in the image space and patient space.

Methods We designed and developed a projector-camera system (PCS) attached to the distal flange of a robot arm. First, system calibration is performed. Second, the PCS is used to obtain the point clouds of the surface of the patient's head, which are utilized for patient-to-image registration. Finally, VAR is produced by merging the real-time video of the patient and the preoperative three-dimensional (3D) operational planning model. In addition, SAR is implemented by projecting the planning electrode trajectories and local anatomical structure onto the patient's scalp.

Results The error of registration, the electrode EPs and the target points are evaluated on a phantom. The fiducial registration error is 0.25 ± 0.23 mm (max 1.22 mm), and the target registration error is 0.62 ± 0.28 mm (max 1.18 mm). The projection overlay error is 0.75 ± 0.52 mm, and the TP error after the pre-warped projection is 0.82 ± 0.23 mm. The TP error caused by a surgeon's viewpoint deviation is also evaluated.

Conclusion The presented system can help surgeons quickly verify registration accuracy during SEEG procedures and can provide accurate EP locations and internal structural information to the surgeon. With more intuitive surgical information, the surgeon may have more confidence and be able to perform surgeries with better outcomes.

Keywords Stereoelectroencephalography · Augmented reality · Viewpoint deviation · Surgical robot · Projector-camera system

Introduction

Image-guided minimally invasive stereoelectroencephalography (SEEG) electrode implantation surgeries are now being accepted by more surgeons [1,2]. Robot-assisted SEEG systems that have the potential to provide faster and more accurate position and orientation information are being increasingly developed [3,4]. However, existing robot-assisted systems are primarily based on preoperative planning trajectories and intraoperative registration to ensure safe and efficient operations [5]. The surgeon can only observe the planning model on the monitor when operating on a patient, and therefore, the entire implantation procedure is not intuitive [6–8].

✉ Guangzhi Wang
wgz-dea@tsinghua.edu.cn

Bowei Zeng
cbw14@mails.tsinghua.edu.cn

Fanle Meng
mengfanle@gmail.com

Hui Ding
dinghui@tsinghua.edu.cn

¹ Department of Biomedical Engineering, School of Medicine, Tsinghua University, Beijing 100084, People's Republic of China

In current SEEG electrode implantation surgeries, only a few feature points can be obtained from the surface of a patient's head in the intraoperative scene for registration [3, 9]. Therefore, the content of the image space is primarily derived from preoperative slices and models (e.g., data derived from computed tomography (CT) or magnetic resonance imaging (MRI)), and it is difficult for the surgeon to intuitively correlate the preoperative image data with the intraoperative scene [6]. Furthermore, to ensure that the registration accuracy meets the needs of the surgery, surgeons often require a long period of time to adjust the registration markers until the registration error is acceptable [9]. Even then, surgeons are unable to confirm the local registration error among registration markers. Therefore, the questions arise of how to help surgeons better determine whether the preoperative three-dimensional (3D) image models correspond to the patient in the intraoperative scene, how to quickly ensure the registration accuracy meets the requirements of the surgery, and how to perform intuitive post-registration verification. Moreover, surgeons also need to be able to identify difficulties that may be encountered before the electrodes are implanted according to preoperative planning trajectories. Overcoming these issues remains extremely challenging.

To achieve bidirectional verification and to enhance information presentation while avoiding interference with normal surgical procedures, we will utilize video see-through augmented reality (VAR) and spatial augmented reality (SAR) techniques [6, 10]. Bidirectional verification can be defined as verification both in the image space and patient space. VAR uses a camera to capture a video and merges the surgical scene video with the preoperative model on the monitor. VAR can render the model more vivid, record the surgical procedures and be observed simultaneously by many surgeons. However, surgeons must be able to correlate the image scene with the surgical scene. SAR overcomes this disadvantage by incorporating a projector to display the anatomical structure directly onto the skin and providing the observer with intuitive internal information through direct superimposition [6]. However, when displaying the interior structure on the surface, both VAR [11] and SAR [12] must consider the user's viewpoint. The use of a tracking device may be uncomfortable for the user and causes a viewpoint deviation between the user's viewpoint and the tracking device [13, 14]. Therefore, the target point (TP) error based on the viewpoint deviation should be studied.

This study aims to allow surgeons to preview the procedure of SEEG implantation on a monitor and to quickly and intuitively verify the registration accuracy. We use a project-camera system (PCS) to obtain point clouds of the patient's head surface. Then, we use VAR in the image space and SAR in the surgical scene to help the surgeon understand the patient's 3D information.

Methods

In this section, we introduce the system components and various technical points. Later, we derive the viewpoint deviation based on a theoretical analysis and propose the corresponding assessment methods.

System introduction

The prototype system contains a PCS, a guiding tube, a six degree of freedom robot arm, a personal computer (PC) and a monitor, as shown in Fig. 1. The PCS is composed of a Pico projector and a compact color camera. The PC functions as a control center with software that controls the functions of the entire system. A live video stream from the camera is transferred to the PC, and VAR is shown on the monitor. The surgeon can select the desired viewpoint in the image space and obtain the content to be projected by taking a screenshot from the monitor. Then, the PC controls the robot arm to move to the exact pose, and the projector projects the captured screenshot on the patient's head, thus realizing the SAR view.

The AR view is realized in three steps. The system is first calibrated, which includes PCS calibration and hand-eye calibration. Second, using the hand-eye calibration parameters $T_c^{R_f}$, the point clouds acquired from the PCS can be transformed to robot arm base coordinates (O_{R_b}). Then, the point clouds are aligned with the preoperative model to obtain the transformation matrix $T_{R_b}^{I_m}$. Therefore, the preoperative surgical plan can be mapped to the patient space. Finally, according to the real camera's pose, we set the virtual camera's pose on the monitor to realize VAR. Then, according to the virtual camera's pose, we set the robot arm's pose to realize SAR. The robot arm can also guide the position and orientation of the electrode trajectories for the surgeon.

Next, we introduce the main technique used to realize the AR view: system calibration, registration and augmented reality with the robot arm.

System calibration

PCS calibration

The PCS is an active structured light technique system [15], which is a principal 3D surface imaging method. The projector projects coded sequences to the object, and the camera simultaneously captures images. The images are then decoded, and the corresponding pixel pairs between the camera image plane and the projector image plane can be found. Thus, the 3D surface point clouds can be reconstructed based on triangulation [16]. However, the intrinsic parameters of the camera (K_c), the projector (K_p) and the transformation matrix (T_c^P) between them must first be calibrated. In [17], a

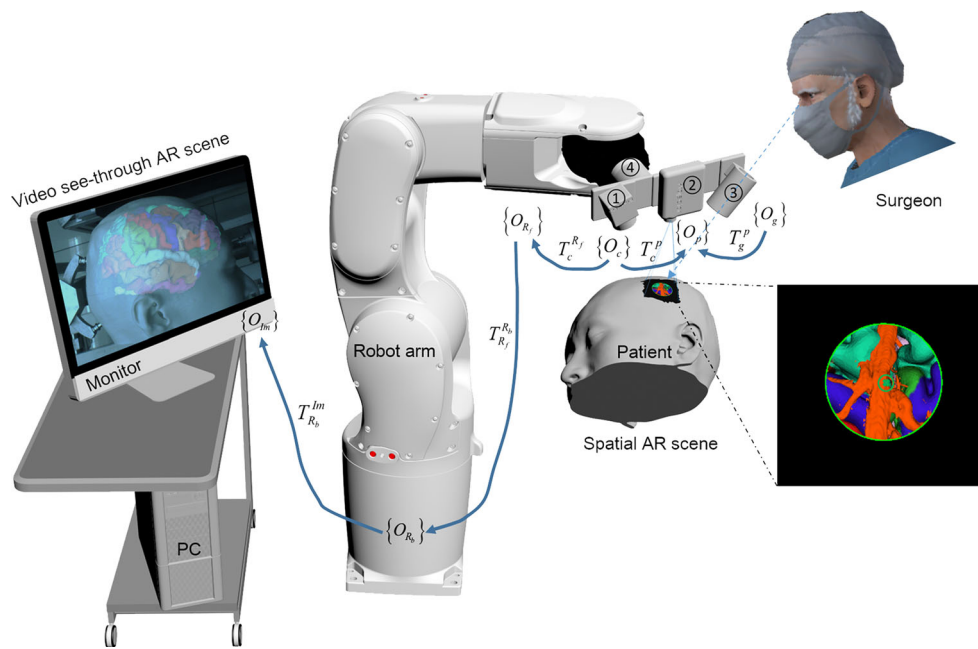


Fig. 1 Overview of the proposed system. Solid line arrows denote rigid transforms. ①: camera, ②: projector, ③: guiding tube, ④: robot arm distal flange

method of calibrating the PCS is proposed, and high calibrating precision was obtained. Therefore, this method is used. Gray code sequences were used for PCS calibration because they were robust and high precision. The PCS calibration can be used to obtain the object's surface point clouds.

Hand-eye calibration

Once the PCS is attached to the robot arm flange, the PCS can move flexibly and obtain the object's surface in robot arm base coordinates (O_{Rb}). To convert the 3D surface data acquired by the PCS from its reference coordinates (selected as camera coordinates (O_c) in this paper) to robot arm base coordinates (O_{Rb}), the transformation matrix from the camera coordinates to robot arm flange coordinates (O_{Rf}) must be calibrated, referred to as hand-eye calibration. There are several effective solutions for hand-eye calibration, but Tsai's method [18] is simple and effective and is used in this paper.

United calibration strategy

Notably, both the method in [17] and Tsai's method require the camera to be calibrated by a known reference object. Zhang's method [19] can generally be used to calibrate the camera. However, as the camera is usually calibrated separately by PCS and hand-eye calibration with different photos, the camera coordinates obtained by the two methods will not coincide. This will cause the 3D point clouds to be joined from different poses with some mismatch. Therefore, we

designed a united calibration strategy to ensure that the calibration of the camera coordinates coincided.

The calibration strategy is shown in Fig. 2. We first placed a chessboard calibration plate around the robot arm in a suitable and fixed position. Then, we maneuvered the robot arm to an appropriate pose and obtained the transformation matrix T_{Rf}^{Rb} from robot arm flange coordinates (O_{Rf}) to robot arm base coordinates (O_{Rb}) from the robot arm controller. The projector projected coding patterns, while the camera captured photos. When n coding pattern projections and camera acquisitions were completed, the pose of the robot arm was changed to a new position. We repeated the above process until we finished m sets. Then, K_c , the extrinsic parameters of camera T_c , K_p , and the transformation matrix T_c^p from camera coordinates (O_c) to the projector coordinates (O_p) were obtained. T_c^p was defined as follows:

$$T_c^p = \begin{bmatrix} R_c^p & t_c^p \\ 0 & 1 \end{bmatrix}, \quad (1)$$

where R_c^p is the rotation and t_c^p is the translation. Using Tsai's method to solve the hand-eye calibration problem, we then obtained the transformation matrix T_c^{Rf} from camera coordinates (O_c) to robot arm flange coordinates (O_{Rf}).

Registration

To map preoperative planning to the patient space, the robot arm base coordinates (O_{Rb}) should be aligned with the image

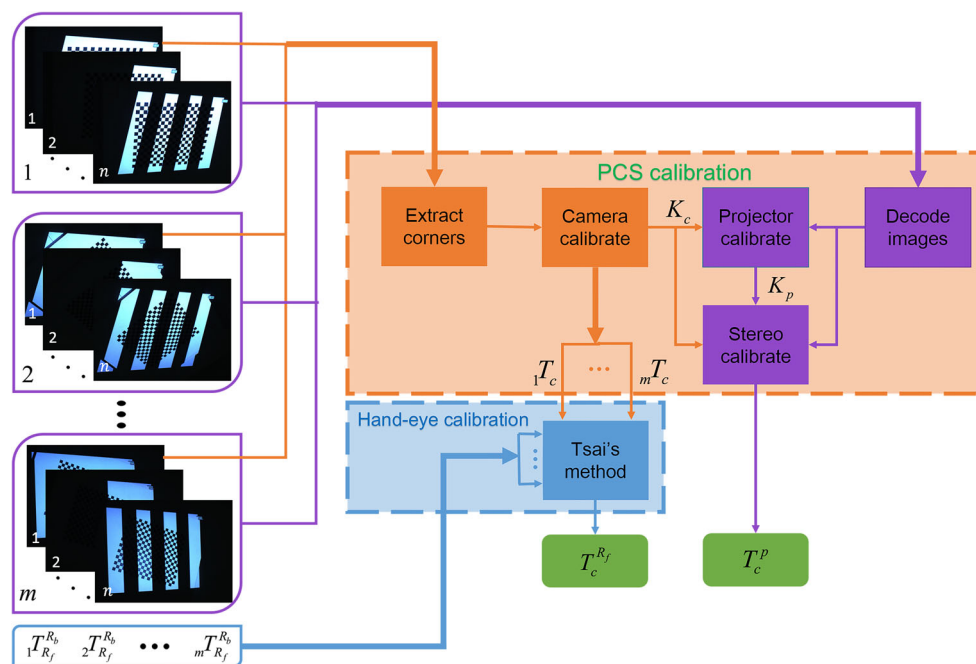


Fig. 2 United calibration strategy

space coordinates of the patient (O_{Im}). We can use the iterative closest point (ICP) [20], which can effectively register 3D points. However, ICP can easily fall into a local minimum and, therefore, requires that the initial position of the two point sets is sufficiently close. There are different distance metrics for ICP error. In general, the point-to-plane distance metric is superior to the point-to-point distance metric [21], and thus, we apply the former.

As the PCS is attached to the robot arm flange, a large surface area of the patient's head can be covered with point clouds from multiple poses. This is helpful for obtaining a more accurate registration transformation matrix. We use manual coarse registration and ICP fine registration to achieve registration from patient to image and set the transformation matrix as $T_{R_b}^{Im}$.

Augmented reality with robot arm method

Fusion presentation by VAR

The robot arm base coordinates (O_{R_b}) and the image space coordinates (O_{Im}) are aligned after registration. To realize VAR, the transformation matrix from the real camera coordinates (O_c) to the virtual camera coordinates (O_{vc}) must be derived. To correspond the virtual camera to the real camera, their parameters should be the same. Therefore, the intrinsic parameters of the virtual camera are assigned as K_c , and the extrinsic parameters are defined by T_{vc}^{Im} :

$$T_{vc}^{Im} = T_{R_b}^{Im} T_{R_f}^{R_b} T_c^{R_f} \quad (2)$$

In this way, the video stream produced by the camera and the preoperative models can be accurately superimposed on the monitor. With the movement of the robot arm ($T_{R_f}^{R_b}$ changes), the virtual camera will update the spatial position of the model in real time. Thus, the surgeon can observe the preoperative model superimposed on the surface of the patient's head on the monitor.

Project surface information by SAR

To project information from the image space onto the patient, the parameters of the virtual camera and the projector should be consistent. Thus, the intrinsic parameters of the virtual camera are assigned as K_p . In addition, the virtual camera's extrinsic parameters T_{vc}^{Im} can be adjusted by selecting the desired perspective to be observed in the image space. Then, the screenshot can be used to obtain the content that will be projected. As the projector is mounted on the robot arm, we also need to derive the corresponding robot arm's pose, which can be calculated as:

$$T_{R_f}^{R_b} = \left(T_{R_b}^{Im}\right)^{-1} T_{vc}^{Im} T_c^P \left(T_c^{R_f}\right)^{-1} \quad (3)$$

Therefore, when adjusting the virtual camera (T_{vc}^{Im} changes), the robot arm will follow the virtual camera to the appropriate location and can then project electrode EPs onto the scalp.

Projecting the internal anatomical structure by SAR

In SEEG implantation, projecting electrode trajectories and the surrounding intracranial blood vessels and cortical structure information onto the scalp before skull drilling would be useful to the surgeons for confirming the EP position. Based on the principle of light linear propagation, the picture that will be projected must be pre-warped by a homography according to the observer's viewpoint so that the observer can see the correct position of the inner structure corresponding to its exact inner position.

As the surgeon is guided by the guiding tube during skull drilling, the surgeon's viewpoint follows the guiding tube. Thus, the surgeon's viewpoint is known. According to the CAD model or the tool calibration method, the transformation matrix $T_g^{R_f}$ from the guiding tube coordinates (O_g) to the robot arm flange coordinates (O_{R_f}) can be obtained. Therefore, the transformation matrix from guiding tube coordinates (O_g) to projector coordinates (O_p) is T_g^p :

$$T_g^p = T_c^p (T_c^{R_f})^{-1} T_g^{R_f} \quad (4)$$

For the verification experiment, we assumed that the guiding tube coordinates (O_g) and the camera coordinates (O_c) coincide, which gives $T_g^p = T_c^p$.

It is possible to display the relevant contents around the electrode trajectory on the scalp within an appropriate area diameter. It is assumed that the display area on the scalp can be approximated by a plane. In the image space, the EPs and TPs can be obtained according to the preoperative planning electrode trajectories. The spatial coordinates of the EPs are $X_{\pi i} = \{x_{\pi i}, y_{\pi i}, z_{\pi i}\}$, $i = 1, \dots, L$, and those of the TPs are $X_{ei} = \{x_{ei}, y_{ei}, z_{ei}\}$, $i = 1, \dots, L$, where i denotes the sequence of the electrodes and L denotes the number of electrodes. The direction of the viewpoint can be calculated:

$$v_{\pi ei} = \frac{X_{ei} - X_{\pi i}}{\|X_{ei} - X_{\pi i}\|^2}, \quad i = 1, \dots, L \quad (5)$$

For the i th electrode trajectory, it is assumed that the approximated plane is $P_{\pi i}$, whose normal vector is n_i which can be estimated by a small region around $X_{\pi i}$.

For the i th electrode trajectory in the image space, the virtual camera's projection direction is the viewpoint direction $v_{\pi ei}$. It is assumed that the position of the virtual camera coordinates (O_{vc}) is in the direction of $-v_{\pi ei}$ and that the distance d mm is far away from $P_{\pi i}$. To guide the electrode implantation, the robot arm flange pose can be calculated as:

$$T_{R_f}^{R_b} = T_{im}^{R_b} T_{vc}^{im} (T_c^{R_f})^{-1} \quad (6)$$

The pre-warped image is prepared next. As the plane $P_{\pi i}$ is transformed to camera coordinates (O_c), it is denoted $P_{c\pi i}$, and the normal vector is:

$$n_{ci} = R_{R_f}^c R_{R_b}^{R_f} R_{im}^{R_b} n_i \quad (7)$$

Additionally, the distance from the camera coordinates (O_c) to $P_{c\pi i}$ is still d mm. Let the camera coordinates (O_c) be the reference coordinates. Therefore, the projective matrix of the camera is $M_c = K_c [I \ 0]$, and the projective matrix of the projector is $M_p = K_p [R_c^p \ t_c^p]$. Then, the homography is H_c^p [20]:

$$H_c^p = K_p (R_c^p - t_c^p n_{ci}^T / d) K_c^{-1} \quad (8)$$

The screenshot is then transformed to the pre-warped image by the homography. The projector can finally be used to display the pre-warped image onto the surface, and the camera can be used to capture a photo. By comparing the difference between the images of the real scene and the projected scene, the pre-warped projection accuracy can be evaluated.

Evaluating the viewpoint deviation

The projected picture must be pre-warped so that the inner model projected on the surface from a given viewpoint is in the correct location, as shown in Fig. 3. In the previous section, we assume that the projection is on a surface $P_{c\pi i}$. As the inner TP e is below $P_{c\pi i}$, if an observation is made from the same position as the projector coordinates (O_p), then the exact EP on the surface is the intersection o' . In SEEG context, if the surgeon observes from a given viewpoint in camera coordinates (O_c), then we can pre-warp the screenshot picture and project it at the exact place o . However, if the surgeon moves his head to another position in

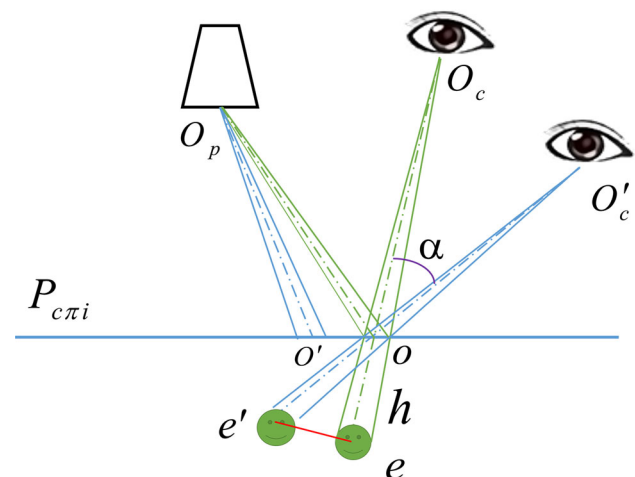


Fig. 3 The viewpoint deviation leads to TP error behind the surface

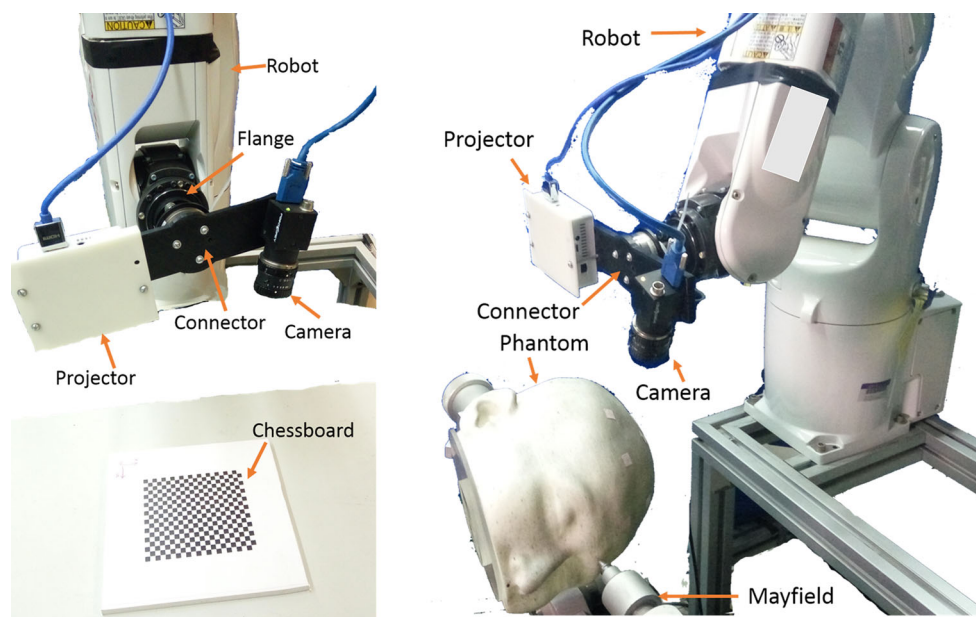


Fig. 4 Calibration and verification experimental setup

camera coordinates (O_c'), the position of his head will not be tracked, and the projection EP will remain at o . Therefore, the surgeon will regard the error target e' as the position of the target. This is most important factor leading to viewpoint deviation.

If the angle deviation is α , the TP error for a TP with depth h can be derived as:

$$d_e^{e'} = h\sqrt{2 - 2\cos\alpha}, \quad (9)$$

where $0 \leq \alpha \leq \pi$, $0 \leq h$. When $h = 0$, the TP is on the surface, and the error is $d_e^{e'} = 0$, which will correspond to no error from any viewpoint. However, when $h > 0$, the TP is below the surface; if the observation angle is fixed, then $d_e^{e'}$ and h are linear. When h is invariant, $d_e^{e'}$ is a monotone increasing function about α . Additionally, the observer can follow the given viewpoint while only changing the distance to the EP. According to Eq. (8), the homography matrix H_c^p changes as the distance from the viewpoint to the plane changes, while the other values remain unchanged. Therefore, the projected area of the object, which the observer sees from the surface, decreases as the distance increases. However, the position of the EP will not change.

Experiment and results

Experimental setup

A robot arm (VS060A3, Denso Co. Ltd., Japan, repeated precision 0.02 mm), a digital color camera (BFLY-U3-50H5M-C, FLIR Integrated Imaging Solutions, Inc.), a video

projector (UC50, Sichuan Dowlab Electronics Technology Co. Ltd., China) and a computer were used in the experiment. The PCS was attached to the robot arm flange by a home-made connector. A chessboard was fixed at a suitable position around the robot base. All calibration data were processed in MATLAB 8.3. Additionally, the application software was developed based on VTK, Qt, PCL and OpenCV. The calibration and verification experimental setup is shown in Fig. 4.

Calibration experiment and results

We first calibrated the PCS, and then we reconstructed the corners of the chessboard as shown in Fig. 5 to verify the accuracy of the PCS with different distances in the working space. The result is shown in Table 1.

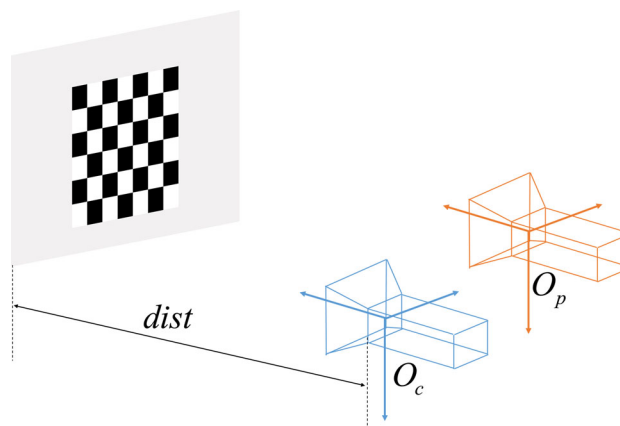


Fig. 5 Reconstruction of the chessboard corners by PCS

Table 1 Reconstruction accuracy of the PCS

Dist/mm	360	400	440	480	520	560
P2P-RMS/mm	0.07	0.04	0.08	0.12	0.17	0.22
P2P-STD/mm	0.04	0.02	0.04	0.06	0.09	0.12
Length_80/mm	79.96	80.01	80.03	80.06	80.07	80.07
Right_angle/°	90.02	89.99	90.01	90.01	90.05	90.11

In Table 1, ‘dist’ is the distance from the camera origin coordinates to the reconstructed chessboard. P2P-RMS and P2P-STD are the root-mean-square and standard deviation from the reconstructed corners to the reconstructed plane, respectively. ‘Length_80’ is the distance of the corners whose theoretical distance was 80 mm. ‘Right_angle’ is the angle of the horizontal and vertical lines. According to Table 1, the distance accuracy of the PCS was better than 0.08 mm, while the angle accuracy was better than 0.12°.

Registration and results

Experimental procedures

A phantom with 13 inner targets was used to evaluate the registration accuracy of the proposed system, as shown in Fig. 6. The phantom originally generated from a patient’s CT data ($512 \times 512 \times 238$ matrix, $0.5 \text{ mm} \times 0.5 \text{ mm} \times 0.8 \text{ mm}$). Then, the head phantom was fabricated using a 3D printer.

The registration experiment was performed in three steps. First, we printed 13 targets on a plastic plate with different heights, and then assembled them inside the head phantom and obtained their CT images. The CT images were used

for extracting the surface model of the phantom. Second, a probe mounted on the end of the robot arm was used to acquire the positions of the targets in robot arm base coordinates. The targets’ positions in the image space were also detected. The PCS was then used to obtain the point clouds of the phantom and register it to the phantom’s surface model. Therefore, the registration transformation matrix T_{Rb}^{Im} can be obtained, and the registration error can be calculated. Finally, the target points from robot arm base coordinates were transformed to the image space by the registration matrix, and the target registration error (TRE) in the image space was calculated by comparing the difference of the two sets of target points.

Results

As the target points were selected manually, we repeated the experiment seven times to reduce human error. The point-to-plane registration errors were regarded as the fiducial registration error (FRE). All results as shown in Table 2. The mean FRE is $0.25 \pm 0.23 \text{ mm}$ (max error 1.22 mm), and the mean TRE is $0.62 \pm 0.28 \text{ mm}$ (max error 1.18 mm).

The distance of each point from the point clouds to the surface model was calculated to obtain the FRE, as shown in Fig. 7a, which illustrates the distribution of registration errors. It is also useful for the surgeon to be able to select arbitrary or interested slices to view the FRE, as shown in Fig. 7b, c. The surgeon can observe the FRE along the slice and zoom area, allowing him to evaluate whether the registration errors meet the requirements of the surgery. In this way, the surgeon can intuitively visualize the FRE with color maps and the region of interest.

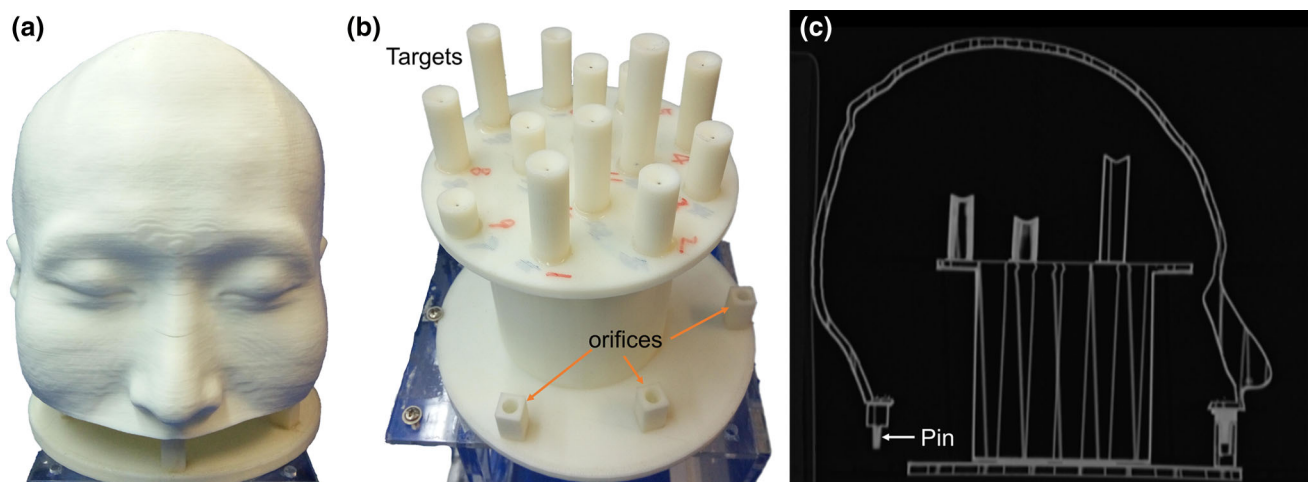
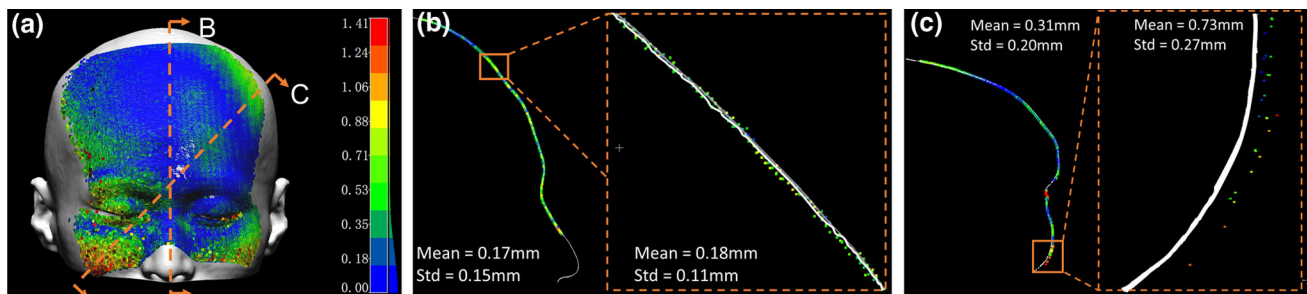


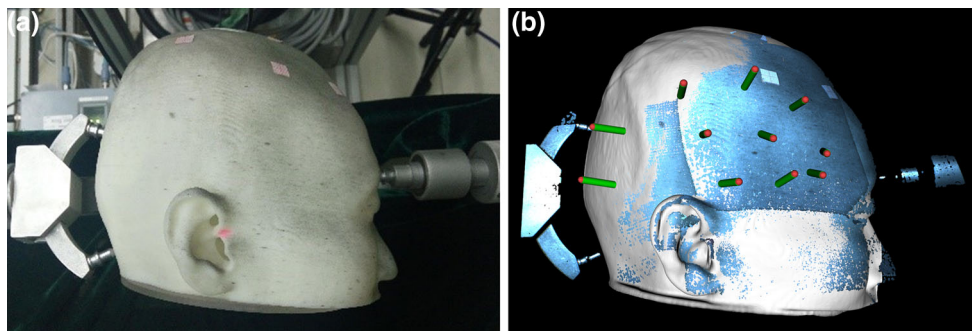
Fig. 6 Registration experiment phantom. **a** Head phantom with targets inside. **b** Targets on a plastic plate connecting with the head phantom by pin-orifice pairs. **c** Head phantom’s CT slice

Table 2 Registration error evaluation

Order	FRE			TRE		
	Max/mm	Mean/mm	Std/mm	Max/mm	Mean/mm	Std/mm
1	1.41	0.21	0.18	1.40	0.68	0.37
2	1.24	0.30	0.27	0.91	0.47	0.24
3	1.05	0.21	0.20	1.29	0.70	0.29
4	1.25	0.26	0.24	1.27	0.71	0.27
5	1.33	0.18	0.15	0.94	0.50	0.22
6	1.12	0.35	0.31	1.26	0.67	0.29
7	1.12	0.25	0.23	1.20	0.64	0.27
Mean	1.22	0.25	0.23	1.18	0.62	0.28

**Fig. 7** Surface registration errors. **a** Point clouds to the surface model registration errors illustrated by color. Slices *B* and *C* are used to further understand the FRE corresponding to **b**, **c**, respectively. **b** The white line (slice *B*) and point clouds overlay well, indicating that the point clouds

have good registration with surface model. The mean values correspond to the mean FRE along the slice, and the Std values are the standard deviations. **c** The obvious overlay error between the white line (slice *C*) and point clouds indicates that they have poor registration at the edge

**Fig. 8** Intraoperative preview in the image space. **a** Fixed phantom in a Mayfield device. **b** The planned electrode trajectories, intraoperative point clouds and phantom preoperative model

Augmented reality realization with the robot arm

Experimental description

The experimental setup shown in Fig. 4 was used to simulate a surgical scene. The phantom was fixed in a Mayfield device, as shown in Fig. 8a. The PCS acquired point clouds of the phantom and its surrounding environment from multiple angles following movement of the robot arm flange. We performed a coarse registration by manually selecting various pairs of points and then used ICP for fine registration.

The patient-to-image transformation matrix $T_{R_b}^{Im}$ was then obtained.

Intraoperative preview

As shown in Fig. 8b, the preoperative planning electrode trajectories, preoperative model and intraoperative point clouds can be simultaneously visualized. The green cylinders indicate electrodes to allow surgeons to intuitively preview the possible surgical scene if they perform the operation according to the current surgical planning. Furthermore, the

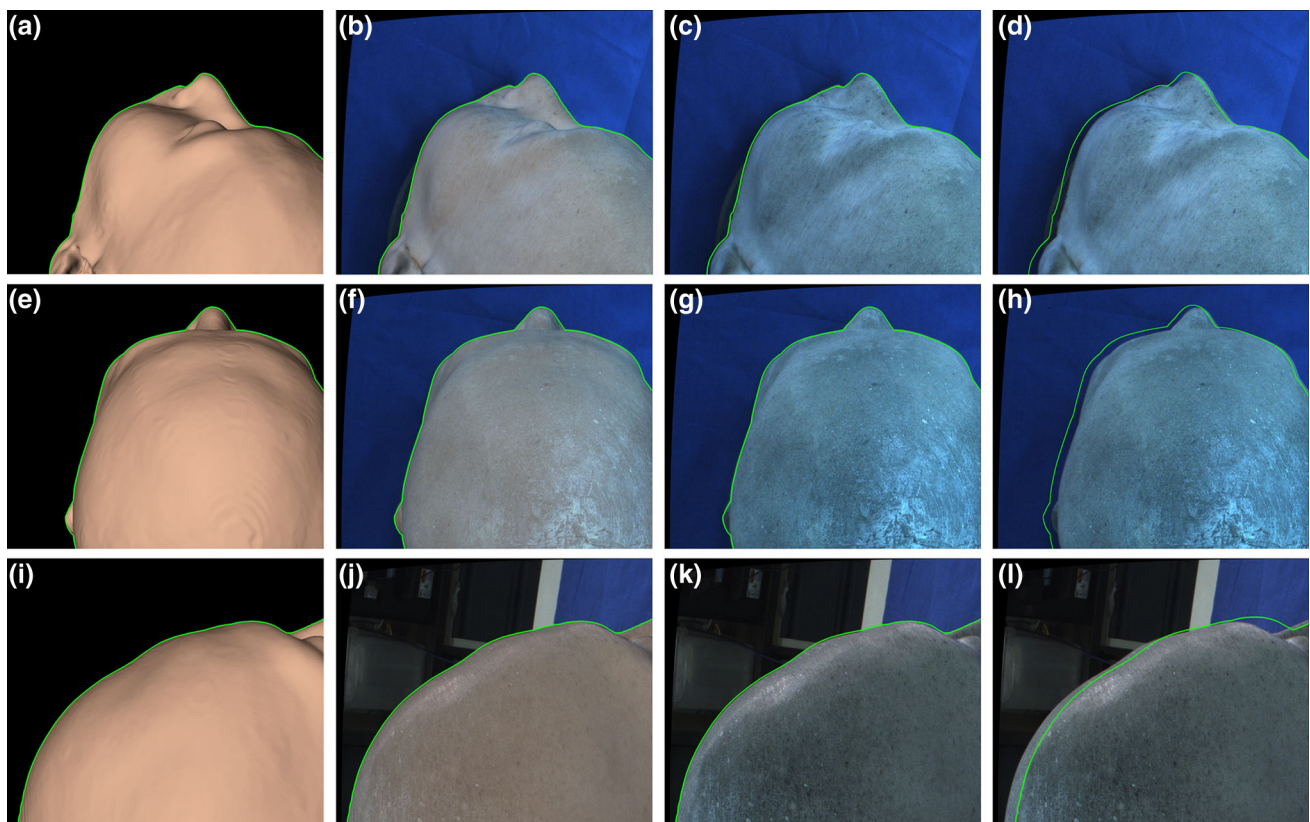


Fig. 9 Confirmation of the registration result by VAR. **a** Viewing from the *left side*. The *green curve* is the contour of the head model from the CT scan in the image space. **b** The head model with 50% opacity is overlaid on the experimental scene from the camera image. **c** The opacity of the head model is set to zero, and therefore, it is invisible. The contour (*green curve*) overlays well with the head phantom from the

camera image. **d** The extrinsic parameter of the virtual camera in the image space with translation offsets in the x , y and z axes is 4.12 mm, -3.45 mm, and -2.65 mm, respectively. The offset between the contour (*green curve*) and the head phantom in the camera image is obvious. **(e–h)** View from the upper direction. **i–l** View from the *right side*. The experimental settings are the same as the view from the *left side*

surgeons can easily verify whether the Mayfield device or any other devices around the patient interfere with the electrode trajectories, allowing the surgeon to change the patient's position and recalculate the registration.

VAR verification

To more intuitively evaluate the registration correctness, the camera attached to the robot arm can be used to view the phantom in different poses. The video stream from the camera can be transferred to the monitor, and the surgeon can observe a VAR, as shown in Fig. 9.

The experiment was performed in the following steps. Registration from the robot arm base coordinates to the image space coordinates was first completed. Second, the camera was used to view the head phantom from the left, upper and right directions to obtain the surgical scene. The screenshot of head model was obtained in the image space, and the contour (*green curve*) of the head model was extracted from the screenshot, as shown in Fig. 9a, e, i. Then, the head model

and its contour were overlaid with the images from the camera at each direction, as shown in Fig. 9 (b, c, f, g, j, k). The contour was extracted by the OpenCV's *canny()* function, which was implemented by the CPU. Third, to better evaluate the registration error, a translation offset (random translation offset ranging from -5 mm \sim $+5$ mm in each axis) was added to the extrinsic parameters of the virtual camera. The second step was repeated 10 times, and one of the results of the VAR with offset was shown in Fig. 9d, h, l. Finally, user feedback was collected from 15 persons with medical backgrounds to evaluate the VAR results. In the user feedback survey, an evaluation score ranging from 1 (good) to 5 (bad) was collected for each picture [22], as shown in Table 3.

Table 3 shows that, after averaging the evaluation scores of views from three different poses, there is a good linear relationship between the translation offset and the average score. This means that surgeon can qualitatively evaluate the registration error by viewing the VAR result from different poses. If the contour curve overlays well with the head phan-

Table 3 Results of the VAR registration qualitative evaluation

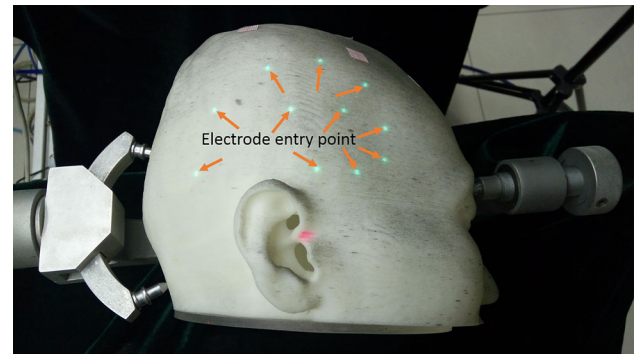
Translation offset*/mm	Left side	Upper	Right side	Average score ^Δ
0	1.15	1.08	1.62	1.28
1.83	1.15	2.62	2.62	2.13
2.48	1.46	2.77	3.15	2.46
3.16	3.69	1.08	3.77	2.85
3.71	3.62	3.15	1.62	2.79
4.41	2.62	3.00	3.31	2.98
5.03	4.23	3.85	1.69	3.26
5.99	1.77	4.38	4.54	3.56
6.84	3.69	2.38	4.08	3.38
7.92	3.54	4.38	4.08	4.00

* Translation offset = $\sqrt{(dx)^2 + (dy)^2 + (dz)^2}$, $dx, dy, dz \in [-5\text{ mm}, 5\text{ mm}]$

^Δ Evaluation score from 1 to 5, corresponding to good to bad

Table 4 Results of the projection precision

Max. error	Mean error	Standard deviation
1.53 mm	0.75 mm	0.52 mm

**Fig. 11** Showing multiple electrode EPs on the phantom surface

tom over a wide range, then the registration should be good. If not, it indicates that a visible registration error still exists. Therefore, the surgeon can easily understand the registration error.

To evaluate VAR accuracy, we used a chessboard fixed at a suitable position around the robot base. The evaluation process involved seven steps: (1) capturing images from multiple poses and recording the transform matrix $T_{R_f}^{R_b}$; (2) extracting the corners of each captured image [23]; (3) calculating the extrinsic parameters of the camera in each pose; (4) separating the data into two sets: a training set and a testing set; (5) calculating the transformation matrix $T_{R_b}^{Im}$ from the training set to the chessboard corners in the image space; (6) transforming the testing set to the image space by $T_{R_b}^{Im}$ as the testing corners; and (7) calculating the difference (overlay errors) between the testing corners and the chessboard corners in the image space [24].

We captured VAR images across the entire working space of our system to evaluate VAR accuracy. VAR's overlay accuracy was 0.54 ± 0.23 mm (max error 0.99 mm).

Evaluating the precision of the projection image on the surface

To evaluate the accuracy of the system, we constructed the experimental environment shown Fig. 10a. Ten markers were made with coordinate paper and placed on the phantom, and the centers of the markers were selected in the image space, as shown in Fig. 10b. The pose of the robot arm was calculated according to Eq. (3). Then, the projector projected a small point on the surface, as shown in Fig. 10c. By the center-to-center principle, we manually measured the distance between the projected point and the target point using a digital caliper. We repeated the experiment ten times to reduce human error, taking the mean and standard deviation of all markers, as summarized in Table 4.

As shown in Fig. 11, the surgeon can determine the location of the preoperative planning electrode EPs on the phantom surface. The surgeon may add markers to the skin to indicate the implantation procedure.

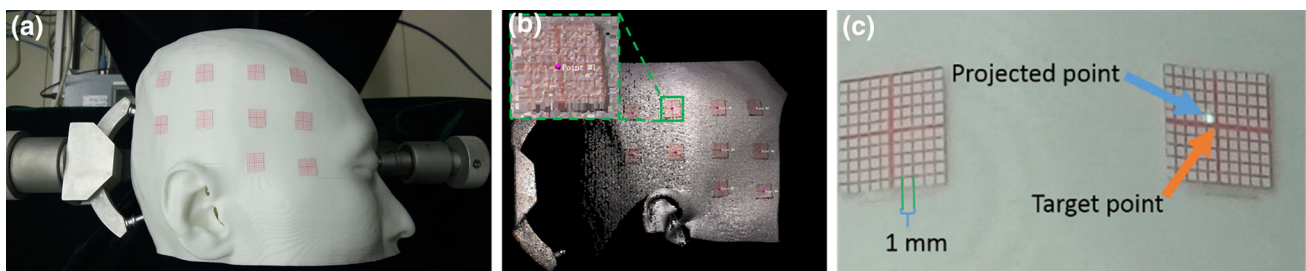
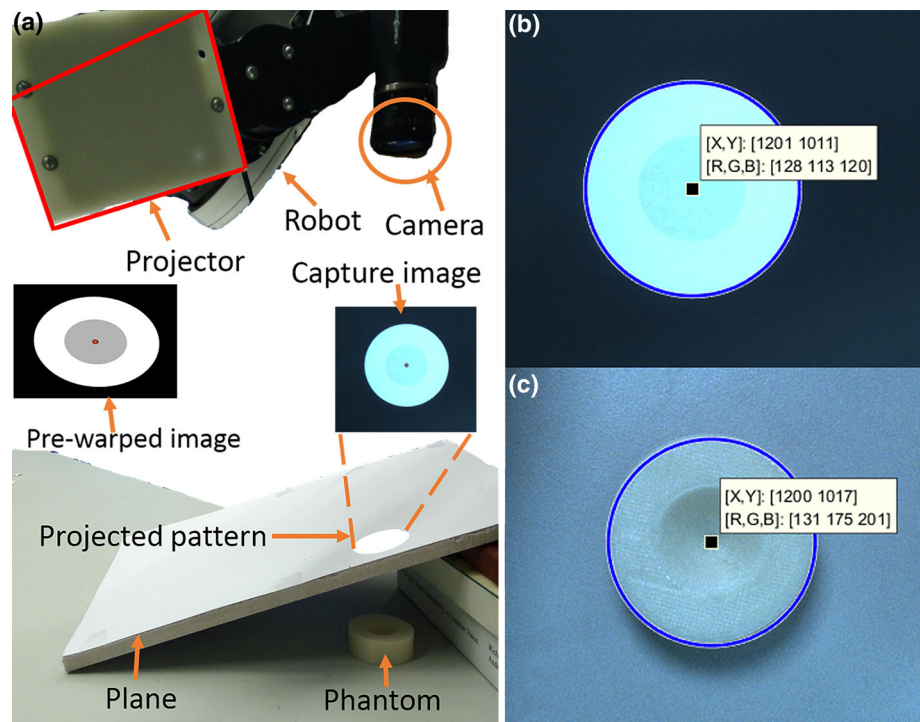
**Fig. 10** Evaluating the projection precision. **a** Experimental setup. **b** Selected markers on the point clouds. **c** Projection of a point on the marker

Fig. 12 Experiment for evaluating the precision of the projection of the inner content on the surface. **a** Experimental setup. **b** Projected pattern captured by the camera. **c** Phantom's photo captured by the camera



Evaluating the precision of projecting the inner content on the surface

Using the experimental setup shown in Fig. 12a, the phantom's CAD model with a radius of 20 mm was generated by SolidWorks. Selecting the center point of the phantom as the TP e , the direction v was defined from top to bottom. Using PCS to acquire the point clouds of the phantom. After aligning the point clouds and CAD model, the registration matrix from robot to image T_{Rb}^{Im} was obtained. In addition, putting an inclined plane above the phantom, the point clouds of the plane (PCP) were acquired. Then, using the matrix T_{Rb}^{Im} to transform the PCP from the robot base coordinates to the image space, the intersection point of the PCP and the line from e along the $-v$ direction was o . Next, the normal vector n_{ci} of the point o was estimated from a small region around it, and the observer's distance d was set to 300 mm. Finally, according to Eq. (8), the homography H_c^p was calculated, and the picture, which is a screenshot from the monitor, was warped. The pre-warping process was performed with OpenCV's *warpPerspective()* function, which is implemented by the CPU.

According to Eq. (6), the robot arm was moved to a suitable pose, the projector displayed the pre-warped image, and the camera captured the scene, as shown in Fig. 12b. The plane was later moved away, and a photo was captured, as shown in Fig. 12c, while the robot arm held the pose. Then, the difference between the center position and the radius of the phantom was evaluated. For a more comprehensive

Table 5 Error of projecting the inner content on different heights of the inclined plane

Height of plane/mm	Error of center/mm	Error of radius/mm
30	0.53	0.54
60	0.88	0.84
90	0.79	0.69
120	1.08	0.43

assessment of the accuracy, we adjusted the height of one side of the inclined plane and repeated the experiment. The result is shown in Table 5. The center error was 0.82 ± 0.23 mm (max 1.08 mm).

Viewpoint deviation estimate

When projecting an EP and a small zone around it, the viewpoint deviation had mainly contributed to the TP error. According to Eq. (9), the TP error was plotted with versus the depth of the target h or the viewpoint deviation α and shown in Fig. 13.

In SEEG electrode implantation surgery, the surgeon's viewpoint is along the guiding tube. If the surgeon's viewpoint deviation is less than 5° , the TP error is less than 2.62 mm for a TP depth of 30 mm.

Some patients require implantations on both sides of their temporal and parietal lobes, and our system is flexible enough

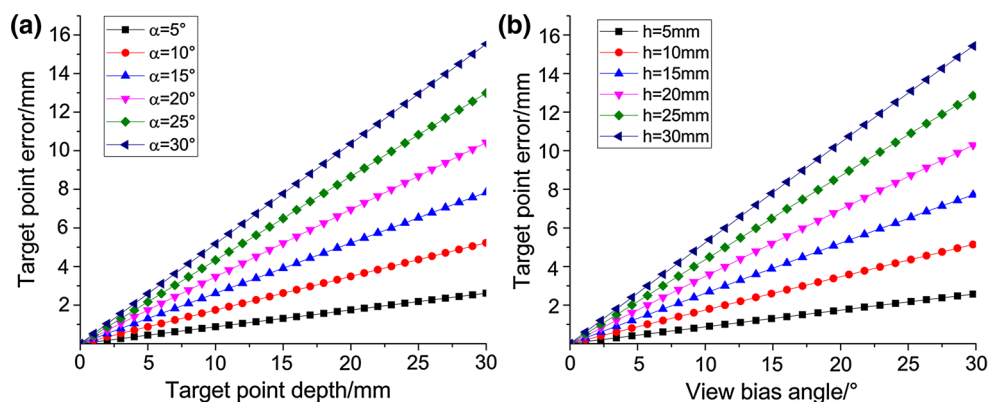


Fig. 13 Evaluation of TP error. **a** TP error and TP depth were linearly related when the viewpoint deviation was invariant **b** TP error was a monotone function of the viewpoint deviation when the TP depth was invariant

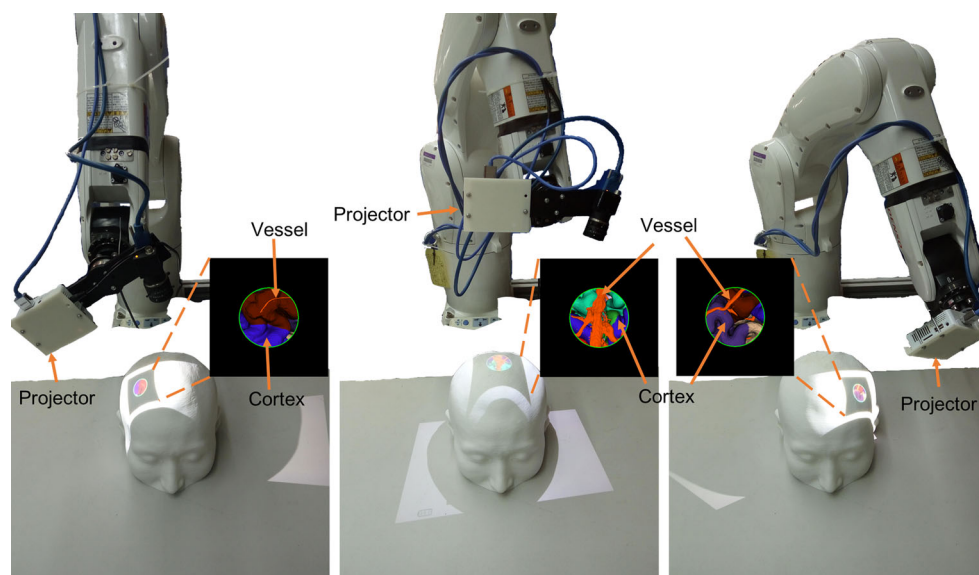


Fig. 14 Flexible guiding and projection from multiple poses

to guide the surgeon from the different required poses, as shown in Fig. 14. To provide better depth perception via the projected image on the surface, we added a dark region around the target [22].

Discussion

Registration accuracy

The PCS can perform high-speed 3D image acquisition that can obtain tens of thousands of points during each acquisition [15]. Compared to the mainstream robot-assisted surgical system [9], our PCS can more quickly and easily obtain a wide range and high density of point clouds for greater registration accuracy. González-Martínez et al. [9] accepted registration errors less than 0.75 mm, and Roessler et al. [25]

suggested that accuracies less than 2 mm were desirable for frameless SEEG. Our FRE is 0.25 ± 0.23 mm (max error 1.22 mm), and TRE is 0.62 ± 0.28 mm (max error 1.18 mm), which are markedly better than the acceptable errors. Vakharia et al. [26] recently performed a systematic review of SEEG accuracy. They summarized mean EP errors of 1.17 mm~2.45 mm and mean TP errors of 1.71 mm~2.89 mm in clinical applications. Our system has an EP error of 0.75 ± 0.52 mm (max error 1.53 mm) and a TP error of 0.82 ± 0.23 mm (max error 1.08 mm). As our experimental results are comparable to or better than clinical results, and therefore, this system has the potential for further development and clinical applications.

AR view

The PCS can realize VAR and SAR without any additional hardware components, representing a major benefit

of our system. After registration, VAR and SAR can be used for bidirectional verification. VAR allows surgeons to move the camera mounted on the robot arm flange to observe the surgical scene merged with preoperative models in the image space on the monitor. This allows surgeons to intuitively evaluate the registration correctness and the preoperative models corresponding to the intraoperative scene [11]. SAR can project the surface of the preoperative model (e.g., the patient's face model extracted from MRI/CT) onto the patient's face to intuitively verify registration correctness. Before drilling, the electrode EP and structures surrounding the electrode trajectory can be projected onto the scalp to help the surgeon confirm the electrode EPs and increase their confidence of drilling. Therefore, SAR can provide intuitive intraoperative guidance to surgeons [27]. VAR and SAR are highly intuitive and useful techniques for assisting surgeons in performing safe and effective operations.

Kockro et al. [11] developed an AR navigation system to register and superimpose multimodality 3D graphics over a live video stream on the monitor. Besharati and Mahvash [6] presented an AR system to directly project virtual images onto the head, skull and brain surface via a video projector. Both groups evaluated their system in intraoperative experiments, which allowed surgeons to directly understand the surgical anatomy beyond the visible surface and provided direct guidance toward the surgical targets. Their successful experiments suggest that our study also has the potential to be tested in clinical experiments and additional applications.

Both VAR and SAR face the viewpoint problem. Kockro et al. [11] described the problem in detail, though the viewpoint deviation problem has not yet been overcome for VAR or SAR. In this study, we evaluated this issue both in theory and in experiments.

To allow the observer to observe if the inner content is projected in the correct position, we can use a tracking device to obtain the observer's viewpoint. However, as we cannot ensure that the tracking device and the user's viewpoint will remain fixed, a deviation will always exist between them. Nevertheless, in SEEG implantation, the surgeon is assisted by a guiding tube when implanting the electrodes. Thus, we can regard the guiding tube as a 'gunsight', such that surgeon's viewpoint is restrained along the guiding tube. This indicates that we do not need to track the surgeon's viewpoint, allowing the surgeon perform the operation without distraction.

Further study

Future studies will work to improve the system, perform clinical tests and expand its applications. Additional features will include developing a better depth perception method and implementing color compensation. When the projected area is a large curved surface, it is necessary to correct the

distortion of the projection pattern and then re-estimate the viewpoint deviation using a curvature surface model rather than the current plane model.

The system can be considered for use in other types of surgeries, such as for epilepsy, brain tumor resection and so on. During surgery, the area of the skull that needs to be opened could be highlighted by a skull excision line projected directly onto the patient's scalp. In resection surgery, the tumor under the brain tissue could be projected onto the scalp or brain surface. Additionally, the relevant functional areas could be projected onto the surface of the brain to guide the surgeon to avoid the erroneous removal of important functional areas.

Conclusion

This paper proposes a prototype surgical robot with a PCS attached to a robot arm flange. The system permits sufficient flexibility of movement to obtain the point clouds of its object from multiple poses. After obtaining the patient-to-image transformation matrix, the intraoperative patient's point clouds can be displayed with the preoperative models and the planning electrode trajectories, allowing the surgeon to quickly verify the accuracy of the registration and preview the scene of the electrode trajectories on a monitor. Additionally, we developed VAR and SAR to make the preoperative and intraoperative scenes more intuitive to the surgeon and to evaluate the accuracy and viewpoint deviation.

Acknowledgements The authors acknowledge the support of the National Natural Science Foundation of China (61361160417, 81271735) and the Ministry of Science and Technology of China (2016YFC0105800, 2017YFA0205904).

Compliance with ethical standards

Conflict of interest The authors declare that they have no conflict of interest.

Ethical approval This article does not contain any studies with human participants or animals performed by any of the authors.

Informed consent This article does not contain patient data.

References

1. Cardinale F, Cossu M, Castana L, Casaceli G, Schiariti MP, Miseroocchi A, Fuschillo D, Moscato A, Caborni C, Arnulfo G (2013) Stereoelectroencephalography: surgical methodology, safety, and stereotactic application accuracy in 500 procedures. *Neurosurgery* 72(3):353–366
2. Cossu M, Fuschillo D, Casaceli G, Pelliccia V, Castana L, Mai R, Francione S, Sartori I, Gozzo F, Nobili L (2015) Stereoelectroencephalography-guided radiofrequency thermocoagulation in the epileptogenic zone: a retrospective study on 89 cases. *J Neurosurg* 123(6):1358–1367

3. Nowell M, Rodionov R, Diehl B, Wehner T, Zombori G, Kinghorn J, Ourselin S, Duncan J, Miserocchi A, McEvoy A (2014) A novel method for implementation of frameless StereoEEG in epilepsy surgery. *Neurosurgery* 10(4):525
4. Faria C, Erlhagen W, Rito M, De Momi E, Ferrigno G, Bicho E (2015) Review of robotic technology for stereotactic neurosurgery. *IEEE Rev Biomed Eng* 8:125–137
5. Tagaytayan R, Kelemen A, Sik-Lanyi C (2016) Augmented reality in neurosurgery. *Arch Med Sci*. doi:[10.5114/aoms.2016.58690](https://doi.org/10.5114/aoms.2016.58690)
6. Besharati Tabrizi L, Mahvash M (2015) Augmented reality-guided neurosurgery: accuracy and intraoperative application of an image projection technique. *J Neurosurg* 123(1):206–211
7. Meola A, Cutolo F, Carbone M, Cagnazzo F, Ferrari M, Ferrari V (2016) Augmented reality in neurosurgery: a systematic review. *Neurosurg Rev*. doi:[10.1007/s10143-016-0732-9](https://doi.org/10.1007/s10143-016-0732-9)
8. Kersten-Oertel M, Gerard I, Drouin S, Mok K, Sirhan D, Sinclair DS, Collins DL (2015) Augmented reality in neurovascular surgery: feasibility and first uses in the operating room. *Int J Comput Assist Radiol Surg* 10(11):1823–1836
9. González-Martínez J, Bulacio J, Thompson S, Gale J, Smithason S, Najm I, Bingaman W (2016) Technique, results, and complications related to robot-assisted stereoelectroencephalography. *Neurosurgery* 78(2):169–180
10. Watanabe E, Satoh M, Konno T, Hirai M, Yamaguchi T (2016) The trans-visible navigator: a see-through neuronavigation system using augmented reality. *World Neurosurg* 87:399–405
11. Kockro RA, Tsai YT, Ng I, Hwang P, Zhu C, Agusanto K, Hong LX, Serra L (2009) DEX - RAY: augmented reality neurosurgical navigation with a handheld video probe. *Neurosurgery* 65(4):795–808
12. Park H, Kang G-C, Lee M-H, Kim S-J, Park J-I (2005) Direct-projected augmented reality considering user's viewpoint. In: *Proceedings of international meeting on information display and exhibition*, pp 748–751
13. Nicolau S, Soler L, Mutter D, Marescaux J (2011) Augmented reality in laparoscopic surgical oncology. *Surg Oncol* 20(3):189–201
14. Hennersperger C, Manus J, Navab N (2016) Mobile laserprojection in computer assisted neurosurgery. In: *International conference on medical imaging and virtual reality*. Springer, pp 151–162
15. Geng J (2011) Structured-light 3D surface imaging: a tutorial. *Adv Opt Phot* 3(2):128–160
16. Hartley R, Zisserman A (2003) *Multiple view geometry in computer vision*. Cambridge University Press, Cambridge
17. Moreno D, Taubin G (2012) Simple, accurate, and robust projector-camera calibration. In: *2012 Second international conference on 3D imaging, modeling, processing, visualization & transmission*. IEEE, pp 464–471
18. Tsai RY, Lenz RK (1989) A new technique for fully autonomous and efficient 3D robotics hand/eye calibration. *IEEE Trans on Robot Autom* 5(3):345–358
19. Zhang Z (2000) A flexible new technique for camera calibration. *IEEE Trans Patt Anal Mach Intell* 22(11):1330–1334
20. Besl PJ, McKay ND (1992) Method for registration of 3-D shapes. In: *Robotics-DL tentative*. International society for optics and photonics, pp 586–606
21. Rusinkiewicz S, Levoy M (2001) Efficient variants of the ICP algorithm. In: *3-D Digital imaging and modeling*. Proceedings. Third international conference on, 2001. IEEE, pp 145–152
22. Sielhorst T, Bichlmeier C, Heining SM, Navab N (2006) Depth perception—a major issue in medical AR: evaluation study by twenty surgeons. In: *International conference on medical image computing and computer-assisted intervention*. Springer, pp 364–372
23. Cheng O, Guangzhi W, Quan Z, Wei K, Hui D (2005) Evaluating harris method in camera calibration. In: *Engineering in medicine and biology society. IEEE-EMBS 2005. 27th annual international conference of the. IEEE*, pp 6383–6386
24. Zhu C, Liang X, Kockro R, Serra L (2004) Accuracy evaluation of an augmented reality enhanced surgical navigation system. In: *International congress series*. Elsevier, p 1329
25. Roessler K, Sommer B, Merkel A, Rampp S, Gollwitzer S, Hamer HM, Buchfelder M (2016) A frameless stereotactic implantation technique for depth electrodes in refractory epilepsy using intraoperative magnetic resonance imaging. *World Neurosurg* 94:206–210
26. Vakharia VN, Sparks R, O'Keefe AG, Rodionov R, Miserocchi A, McEvoy A, Ourselin S, Duncan J (2017) Accuracy of intracranial electrode placement for stereoelectroencephalography: A systematic review and meta-analysis. *Epilepsia* 58(6):921–932
27. Krempien R, Hoppe H, Kahrs L, Daeuber S, Schorr O, Eggers G, Bischof M, Munter MW, Debus J, Harms W (2008) Projector-based augmented reality for intuitive intraoperative guidance in image-guided 3D interstitial brachytherapy. *Int J Radiat Oncol Biol Phys* 70(3):944–952